Terahertz spectroscopy for all-optical spintronic characterization of the spin-Hall-effect metals Pt, W and $Cu_{80}Ir_{20}$

T. Seifert[1,2], N. M. Tran[3], O. Gueckstock[1], S. M. Rouzegar[1], L. Nadvornik[1,2], S. Jaiswal[4,5], G. Jakob[4,6], V. V. Temnov[3], M. Münzenberg[7], M. Wolf[1], M. Kläui[4,6], T. Kampfrath[1,2*]

1. Department of Physical Chemistry, Fritz Haber Institute of the Max Planck Society, 14195 Berlin, Germany
2. Department of Physics, Freie Universität Berlin, 14195 Berlin, Germany
3. Institut des Molécules et Matériaux du Mans, UMR CNRS 6283, Le Mans Université, 72085 Le Mans, France
4. Institute of Physics, Johannes Gutenberg University, 55128 Mainz, Germany
5. Singulus Technologies AG, 63796 Kahl am Main, Germany
6. Graduate School of Excellence Materials Science in Mainz, 55128 Mainz, Germany
7. Institute of Physics, Ernst Moritz Arndt University, 17489 Greifswald, Germany

* Email: tobias.kampfrath@fu-berlin.de

Abstract. Identifying materials with an efficient spin-to-charge conversion is crucial for future spintronic applications. The spin Hall effect is a central mechanism as it allows for the interconversion of spin and charge currents. Spintronic material research aims at maximizing its efficiency, quantified by the spin Hall angle Θ_{SH} and the spin-current relaxation length λ_{rel}. We develop an all-optical method with large sample throughput that allows us to extract Θ_{SH} and λ_{rel}. Employing terahertz spectroscopy, we characterize magnetic metallic heterostructures involving Pt, W and $Cu_{80}Ir_{20}$ in terms of their optical and spintronic properties. We furthermore find indications that the interface plays a minor role for the spin-current transmission. Our analytical model is validated by the good agreement with literature DC values. These findings establish terahertz emission spectroscopy as a reliable tool complementing the spintronics workbench.

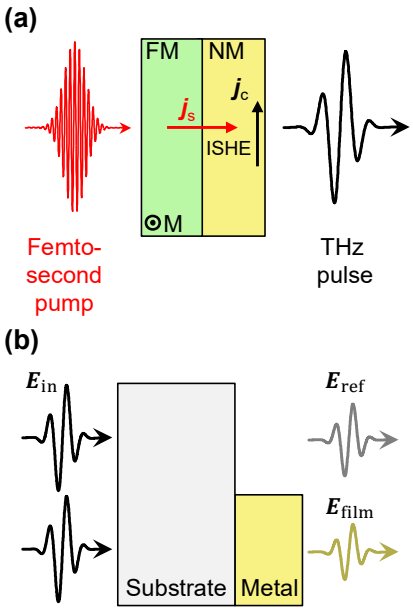

Figure 1. Schematic of the experiment. (a) Terahertz emission experiment. A femtosecond near-infrared pump pulse excites electrons in both the ferromagnetic (FM, in-plane magnetization $\boldsymbol{M}$) and non-magnetic (NM) metal layer. Consequently, a spin current $\boldsymbol{j_s}$ is injected from the FM into the NM material where it is converted into an in-plane charge current $\boldsymbol{j_c}$ by the inverse spin Hall effect (ISHE). This sub-picosecond charge-current burst leads to the emission of a terahertz (THz) pulse into the optical far-field. (b) Terahertz transmission experiment. A THz transient $\boldsymbol{E_{in}}$ is incident onto either the bare substrate or on to the substrate coated by a thin metal film. By comparing the two transmitted waveforms $\boldsymbol{E_{ref}}$ and $\boldsymbol{E_{film}}$, the metal conductivity at THz frequencies is determined.

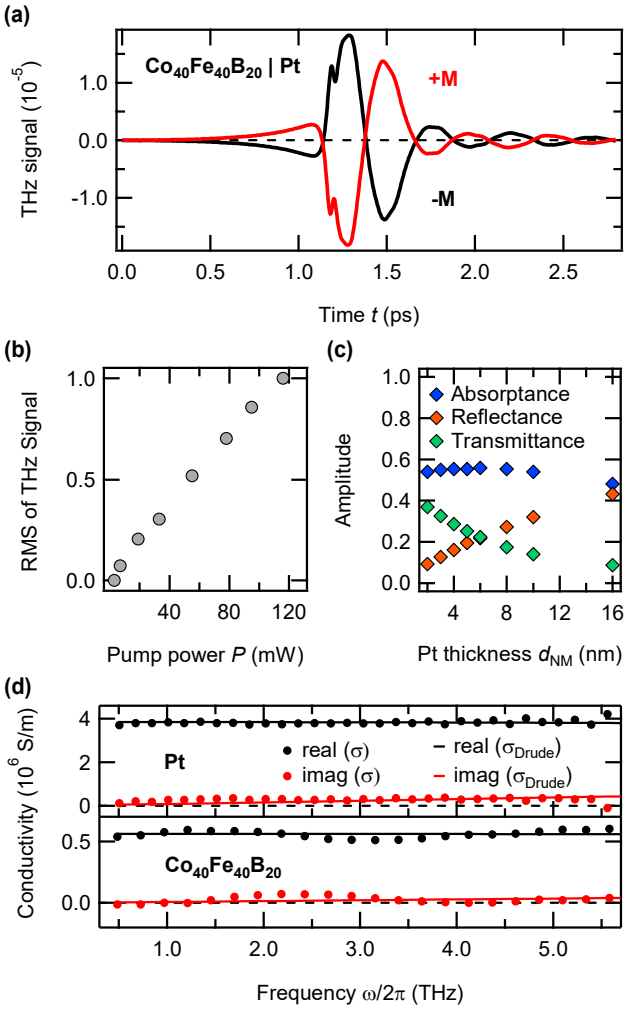

Figure 2. Typical THz emission raw data and sample characterization. (a) THz emission signal measured from a $C_{40}F_{40}B_{20}$(3 nm)|Pt(3 nm) bilayer for two opposite orientations of the sample magnetization ($\pm\boldsymbol{M}$). **(b)** Pump-power dependence of the THz signal amplitude (RMS) for one orientation of the sample magnetization. **(c)** Pump-light absorptance, transmittance and reflectance as function of the Pt-layer thickness. **(d)** Frequency-dependent THz conductivities measured by THz transmission experiments (black and red dots) along with fits obtained by the Drude model (black and red solid lines).

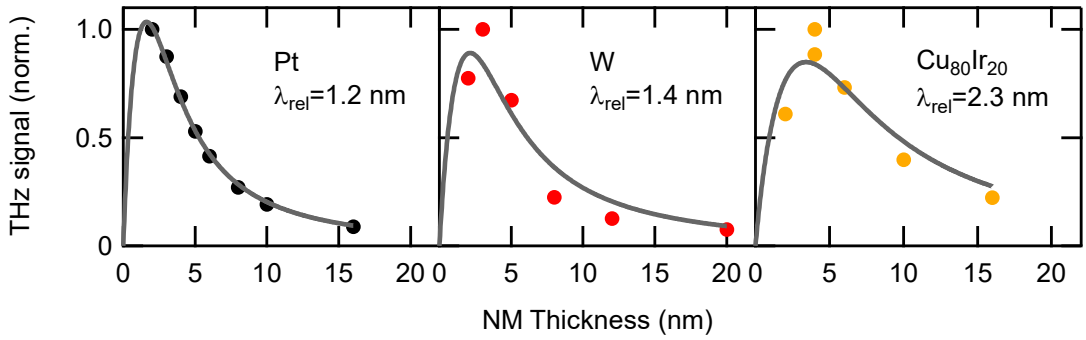

Figure 3. Thickness dependence of the THz-emission signal. THz-signal amplitude (RMS) as a function of the NM layer thickness normalized to the pump absorptance for $Co_{40}Fe_{40}B_{20}$(3 nm)|Pt (markers in left panel), $Co_{20}Fe_{60}B_{20}$(3 nm)|W (center panel), and Fe(3 nm)|$Cu_{80}Ir_{20}$ (right panel). Grey solid lines show fits based on Eqs. (1) and (2) with the relaxation length $\boldsymbol{\lambda_{rel}}$ and a global amplitude as free parameters.

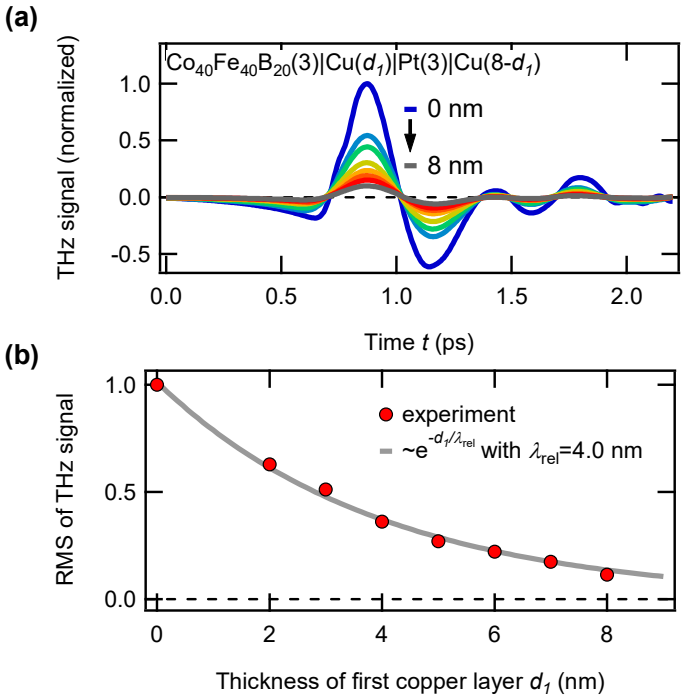

Figure 4. Role of the interface in THz emission studies. (a) THz waveforms emitted from $Co_{40}Fe_{40}B_{20}$|Cu($\boldsymbol{d_1}$)|Pt|Cu(8 nm$-\boldsymbol{d_1}$) structures with fixed $Co_{40}Fe_{40}B_{20}$ and Pt thicknesses of 3 nm and $\boldsymbol{d_1}$ ranging from 0 to 8 nm. **(b)** THz signal amplitudes (RMS) vs $\boldsymbol{d_1}$ together with a single exponential fit $\propto \boldsymbol{\exp(-d_1/\lambda_{rel})}$ with $\boldsymbol{\lambda_{rel}} = 4.0$ nm.

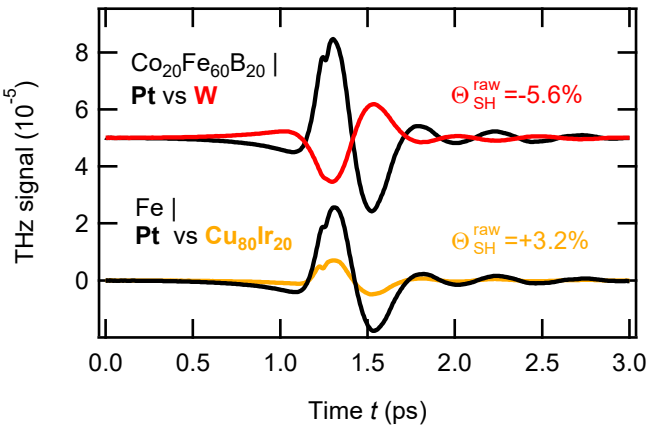

Figure 5. Comparison of raw THz-emission data from Pt, W, and $Cu_{80}Ir_{20}$. THz waveforms emitted from FM|NM structures where NM is W (red) and $Cu_{80}Ir_{20}$ (orange) in comparison to a FM|Pt reference structure with the same layer thicknesses. The values of $\boldsymbol{\Theta_{SH}^{raw}}$ indicate the estimated spin Hall angles of the respective NM materials based on their ratios of THz-signal amplitudes (RMS) and assuming a spin Hall angle of 12.0% for the Pt reference.

Table 1. Overview of samples used for THz-emission measurements together with the corresponding reference samples. Numbers in brackets indicate the film thickness in nm. In the last row, d_1 ranges from 0 to 8 nm. The substrate thickness is 500 µm.

NM material	Sample structure	Reference sample structure
Pt	Glass||$Co_{40}Fe_{40}B_{20}$(3)|Pt(2-16)	-
W	Glass||$Co_{20}Fe_{60}B_{20}$(3)|W(2-20)	Glass||$Co_{20}Fe_{60}B_{20}$(3)|Pt(3)
$Cu_{80}Ir_{20}$	Glass||Fe(3)|$Cu_{80}Ir_{20}$(2-16)|AlO_x(3)	Glass||Fe(3)|Pt(4)
Cu	Glass||$Co_{40}Fe_{40}B_{20}$(3)|Cu(d_1)|Pt(3)|Cu(8-d_1)	-

Table 2. Sample details for THz-transmission measurements. Drude-model fit parameters σ_{DC} and Γ, conductivity literature values σ_{DC}^{lit}, and substrate-thickness variation Δd_{sub}. Numbers in brackets indicate the film thickness in nm. The substrate thickness is 500 µm.

Material	**Sample**	σ_{DC} **(10^6 S/m)**	σ_{DC}^{lit} **(10^6 S/m)**	**Reference**	Γ **($2\pi \cdot 10^{12}$ Hz)**	Δd_{sub} **(µm)**
$Co_{40}Fe_{40}B_{20}$	Glass||$Co_{40}Fe_{40}B_{20}$(3)|MgO(4)	0.6	0.7	[1]	81	-0.1
Pt	Glass||Pt(10)	3.9	5.4	[4]	51	5.8
$Co_{20}Fe_{60}B_{20}$	Glass||$Co_{20}Fe_{60}B_{20}$(6)	0.6	-	-	25	-7.3
W	Glass||W(10)	1.9	2.0	[2]	>100	-5.9
Fe	MgO||Fe(3) |AlO_x(3)	2.7	4.0	[3]	>100	-2.2
$Cu_{80}Ir_{20}$	Glass||$Cu_{80}Ir_{20}$(4)|AlO_x(3)	1.0	2.0	[39]	64	-0.6

Table 3. Spin-Hall parameters. Spin-current relaxation length λ_{rel} along with the literature value λ_{rel}^{lit}. Also given is the ratio of THz emission signals Θ_{SH}^{raw} between a FM/NM heterostructure and the corresponding FM|Pt reference sample as well as the extracted relative spin Hall angle Θ_{SH} corrected for sample specific parameters [see Eqs.(1) and (2)].

NM Material	λ_{rel} **(nm)**	λ_{rel}^{lit} **(nm)**	**Ref.**	Θ_{SH}^{raw} **(10^{-2})**	Θ_{SH} **(10^{-2})**
Pt	1.2	1.1	[4]	12.0	12.0
W	1.4	<3	[17]	-5.6	-4.0
$Cu_{80}Ir_{20}$	2.3	<5	[38]	3.2	1.9

1. Introduction

The use of the electron spin to replace some parts of conventional electronics based on charge dynamics is the goal of spintronics research and holds great promises in terms of future information technology[5]. Its large potential is highlighted by recently developed competitive spintronic applications such as spin-transfer- and spin-orbit-torque magnetic random-access memory[6,7,8]. Driven by fundamental and material-science research at the same time, future progress in spintronics crucially relies on the identification of materials with efficient spin-to-charge-current conversion.

A central effect in this regard is the spin Hall effect and its inverse (ISHE) which transforms a spin into a transverse charge current and vice versa[9,10]. In terms of applications, the conversion efficiency, which can be quantified by the product of the spin Hall angle Θ_{SH} and the spin-current relaxation length λ_{rel}, should be maximized. Therefore, one needs to be able to screen many material candidates efficiently and accordingly optimize spintronic device parameters. To this end, a fast, reliable and straightforward characterization method is thus a key to realize future spin-based applications.

So far, most works relied on electrical measurements which require microstructuring and electrical contacting of the samples[11,12,13,14]. This procedure is costly, time consuming and may complicate data interpretation due to additional contact resistance[15]. Other established techniques like spin-Seebeck-effect measurements do not require microstructuring but still rely on electrical contacting[39]. Recently, non-contact methods have been developed which are based on inductive coupling between a microwave waveguide and the spintronic sample[16] or on magnetooptically detected ferromagnetic resonance[17].

Here, we present an all-optical scheme using terahertz (THz) emission spectroscopy (TES) of metallic heterostructures together with a detailed analysis of how to extract the key quantities Θ_{SH} and λ_{rel}. The operational principle is shown in Fig.1(a): The inversion-asymmetric sample is excited by a femtosecond near-infrared pump pulse, thereby driving an ultrafast spin current from the FM into the NM layer. This process can be considered as an ultrafast version of the spin-dependent Seebeck effect. In the NM layer, the ISHE converts the longitudinal spin flow into a transverse, in-plane charge current[18,19,20,21]. This sub-picosecond transverse charge-current burst leads to the emission of a THz electromagnetic pulse into the optical far-field where it is detected by electrooptic sampling[22,23]. This scenario can also be considered as a realization of the spin-galvanic effect[24].

It is worth noting that THz emission by spintronic multilayers consisting of nanometer-thick ferromagnetic (FM) and nonmagnetic (NM) metals has led to the development of efficient THz emitters[19,25,26,27,28,29] which are capable of providing a broadband and continuous spectrum from 1 to 30 THz without gaps (for details see ref. 19). In addition, we recently found agreement between the amplitude of the THz field emitted from FM|NM bilayers and the intrinsic spin-Hall conductivity of the employed NM material[19]. This observation is, however, surprising because Θ_{SH} and λ_{rel} were shown to be highly dependent on the electron energy[30,31]. Moreover, the spin-current-injection efficiency is material- and interface-dependent[32,33]. These intriguing issues require a more detailed study to establish TES of magnetic heterostructures[34,35,36,37] as a reliable spintronic characterization tool. In the following, we focus onto two familiar spintronic metals, namely platinum and tungsten, as well as a new and promising copper-iridium alloy[38,39].

2. Theoretical background

In analogy to DC-spin-pumping experiments[12], we describe the in-plane sheet charge-current density J_{c} in the NM layer by a simple model which yields[19,20]

$$J_{\mathrm{c}} = \frac{AF_{\mathrm{inc}}}{d} j_{\mathrm{s}}^{0} \cdot \lambda_{\mathrm{rel}} \tanh \frac{d_{\mathrm{NM}}}{2\lambda_{\mathrm{rel}}} \cdot \Theta_{\mathrm{SH}}. \qquad (1)$$

Here, A is the absorbed fraction of the incident pump-pulse fluence F_{inc} (the latter being constant for all measurements throughout this work), d is the entire metal thickness, j_s^0 is the spin-current density (per pump-pulse excitation density) injected through the FM/NM interface into the NM layer, d_{NM} is the NM layer thickness, λ_{rel} is the relaxation length of the ultrafast spin-current, and Θ_{SH} is the spin Hall angle.

Equation (1) accounts for the photoinduced injection of the spin current in the NM layer (first term), the multiple spin-current reflections in the NM layer (second term) and the ISHE (last term). For simplicity, we assume a spin-current reflection amplitude of unity at the NM/air and NM/FM interfaces. Moreover, the spin- and energy-dependent spin-current transmission[32,33] of the FM/NM interface is assumed to be approximately independent of the NM material. This assumption is supported by our previous results in which a strong correlation between THz signal amplitude and the spin Hall conductivity of the NM layer was found (see Fig. 2 in Ref. 19). Since the currents are driven by linear absorption of pump photons [see Fig. 2(b)], we assume that the sheet charge-current density scales linearly with the pump-pulse excitation density A/d.

Finally, to determine the resulting THz electric field, we assume a normally incident plane-wave-like pump pulse and a sufficiently thin metal film (total metal thickness d minor compared to attenuation length and wavelength of the THz field within the metal). Under these assumptions, the THz electric field directly behind the sample reads[19,20]

$$E_{\mathrm{THz}}(\omega) = \frac{eZ_0}{n_1 + n_2 + Z_0 \int_0^d \mathrm{d}z\, \sigma(\omega, z)} J_{\mathrm{c}}(\omega). \tag{2}$$

Here, n_1 and $n_2 \approx 1$ are the refractive indices of substrate and air, respectively, $-e$ denotes the electron charge, $Z_0 \approx 377\ \Omega$ is the vacuum impedance, and σ is the z-dependent metal conductivity at THz frequencies.

It is important to emphasize that Eq. (2) was derived for a collimated pump beam with a diameter much larger than all THz wavelengths considered. Therefore, the THz beam behind the sample can be approximated by a plane wave. This condition is not fulfilled in our experiment (see below) where the pump focus is substantially smaller than the detected THz wavelengths which easily exceed 100 µm. However, as shown in the Supplementary Material, Eq. (2) remains valid within a relative error of less than 3% because the apertures of optical elements after the sample reduce the divergence angle of the THz beam to less than 20° with respect to the optical axis.

Equations (1) and (2) provide the key to determine Θ_{SH} and λ_{rel} and naturally take us to the following three-step procedure: first, we characterize the involved metals in terms of their parameters unrelated to spintronics, namely A and σ [see Fig. 1(b)]. Second, we extract λ_{rel} by varying the NM layer thickness in a THz emission experiment [see Fig. 1(a)]. Third, we address the spin-current transmission of the FM/NM interface. Eventually, the relative spin Hall angle Θ_{SH} is determined by a reference measurement using the widely studied metal Pt as NM layer[40].

3. Experimental details

We employ femtosecond near-infrared laser pulses (central wavelength of 800 nm, duration of 10 fs, energy of 2.5 nJ, repetition rate of 80 MHz) from a Ti:Sapphire laser oscillator to excite the sample under study [see Fig. 1(a)]. In the THz emission experiment [Fig. 1(a)], the pump beam is focused onto the sample (spot size of 22 µm full width of the intensity maximum).The emitted THz pulse is detected by electrooptic (EO) sampling[22,23] in a standard 1-mm-thick ZnTe crystal using a copropagating femtosecond near-infrared pulse derived from the same laser. To saturate the sample magnetization in the sample plane, an external field of 10 mT is applied. All measurements are carried out in a dry nitrogen atmosphere.

For the THz conductivity measurements[41] [Fig. 1(b)], the femtosecond pump pulses are replaced by broadband THz pulses generated in a spintronic THz emitter[19]. We measure the transmission of the THz pulse through the metallic sample film on the substrate and through a part of the substrate free of any metal [see Fig. 1(b) and Supplementary Material for details]. For these THz transmission experiments, we employ a 250-µm-thick GaP EO crystal as detector.

Note that the electrooptic signal of the THz pulse $S(t)$ is in general not simply proportional to the transient THz electric field $E_{\mathrm{THz}}(t)$ [Fig. 1(a)]. Instead, it is a convolution of $E_{\mathrm{THz}}(t)$ with the setup response function which captures the propagation and electrooptic sampling[42,43]. One can, in principle, retrieve the THz field $E_{\mathrm{THz}}(t)$ from the electrooptic signal $S(t)$ to eventually determine the dynamics of the charge current flowing inside the sample[43]. Throughout this study, however, all measurements are carried out under similar experimental conditions, thereby enabling a direct comparison of the measured raw data.

Tables 1 and 2 summarize the detailed stacking structure of the samples used for TES and for THz transmission measurements, respectively. Details on the sample preparation can be found in the Supplementary Material.

4. Results

4.1. Typical THz-emission raw data

Figure 2(a) shows typical THz-emission raw data measured from a $C_{40}F_{40}B_{20}$(3 nm)|Pt(3 nm) bilayer. The signal reverses almost entirely when the sample magnetization is reversed, thus confirming its magnetic origin. For all studied samples, the signal contribution which is even in the sample magnetization is found to be below 5% of the signal odd in the sample magnetization. It might originate from sample imperfections such as pinned magnetic domains[44], but is not considered further as the odd signal clearly dominates. Consequently, we concentrate only on the THz signal for one orientation of sample magnetization.

We observe that the THz-signal amplitude [root mean square (RMS) of the time-domain THz signal] increases linearly with pump fluence. This finding indicates that a second-order nonlinear process in the pump laser field is operative [see Figs. 2(b) and S1]. It agrees with the linear scaling of the THz sheet charge-current density with F_{inc} [see Eq. (1)].

The THz waveforms emitted from all samples exhibit similar temporal dynamics. Thus, a direct comparison of signal amplitudes (RMS) is possible.

4.2. Optical and THz characterization

To isolate the intrinsic spin-orbit-interaction-related parameters from the THz-emission signal, we first measure the optical absorptance of the pump pulse [see Fig. 2(c)]. We note that currents arising from a pump-induced gradient can be neglected for thicknesses smaller than 20 nm because the larger penetration depth of the pump electric field and its multiple reflections result in a constant electric field along the z-direction in the sample[19].

Second, we characterize the samples by THz-transmission experiments[41]. In the thin-film limit, the THz transmission can directly be related to the metal-film conductivity, which we extract in the frequency interval from 0.5 to 5.5 THz. Details of the extraction procedure are described in the Supplementary Material. Note that we treat the multilayers as a parallel connection of their constituents. Therefore, the total conductance of the multilayer is given by the sum of the individual layer conductances.

We find that all metal conductivities are well described by the Drude model [see Figs. 2(d), S3 and the Supplementary Material for details]. The DC conductivity σ_{DC} and electronic velocity relaxation rate Γ are used as fit parameters whose values for all involved materials are given in Table 2. Note that a slight variation in the substrate thickness Δd_{sub} between sample and reference THz transmission measurements are accounted for by a phase-shift term[45,46] of the form $\exp[-\mathrm{i}\omega(n_2-1)\Delta d_{\mathrm{sub}}/c]$ with the free parameter Δd_{sub} (see Table 2).

In the following, we consider the frequency-averaged THz conductivity in which each frequency is weighted by the relative spectral amplitude of the detected THz signal. A comparison of the extracted values of σ_{DC} and literature values $\sigma_{\mathrm{DC}}^{\mathrm{lit}}$ reveals a good agreement (see Table 2). Deviations, such as those in the cases of Fe and $Cu_{80}Ir_{20}$, are most likely caused by different thicknesses[47] or crystallinity of the films. With this procedure, we have determined all parameters unrelated to the spin-to-charge conversion in the NM layer [see Eqs. (1) and (2)].

4.3. Thickness dependence

The first key parameter to be extracted is the relaxation length λ_{rel} of the ultrafast spin current in the NM layer. To this end, we carry out thickness-dependent measurements (see Fig. 3). Here, the FM layer thickness is kept constant and the NM layer thickness is varied. The measured data are scaled by the pump pulse absorptance and normalized to one [see Figs. 2(c) and S2]. A least-square fit using Eqs. (1) and (2), where the only free parameters are λ_{rel} and a global amplitude, yields a λ_{rel} of 1.2 nm for Pt, 1.4 nm for W, and 2.3 nm for $Cu_{80}Ir_{20}$ (see Fig. 3 and Table 3). We find that these values are quite insensitive to the value of the spin-current reflection amplitude at the FM/NM interface, thereby underlining the robustness of our analysis.

The λ_{rel} values inferred here agree very well with literature values from DC experiments (see Table 3) and are consistent with previous THz-emission studies on FM|Pt bilayers[19]. The agreement is surprising as the DC experiments measure the DC spin diffusion length which does not necessarily coincide with the relaxation length of the THz spin current. The latter might be even shorter since spin flips usually occur only in a fraction of all electronic scattering events[48]. Furthermore, we find an inverse proportionality between σ_{DC} (see Table 2) and λ_{rel} (see Table3). However, no correlation between the Drude scattering rate Γ and the relaxation length λ_{rel} is seen. These interesting observations will be addressed in forthcoming studies.

4.4. Role of the FM/NM interface

To gain insights into the role of the interfacial spin-current transmission in the THz emission, we study samples with an intermediate layer with varying thickness. As material, we choose copper as it exhibits a negligibly small SHE[32] and efficient spin current transport[49] that can be employed for spin switching devices[50].

In detail, we measure the emitted THz signal from $Co_{40}Fe_{40}B_{20}$(3 nm)|Cu(d_1)|Pt(3 nm)|Cu(8 nm-d_1) stacks (see Table 1) with d_1 ranging from 0 to 8 nm [see Fig. 4(a)]. This choice of layer structure results in a pump-pulse absorptance of $A \approx 0.6$, largely independent of d_1. Moreover, as seen from Eq. (2), the THz-outcoupling efficiency is independent of d_1. Note that the platinum thickness of 3 nm is sufficient to prevent any sizeable spin-current transmission into the second copper layer (compare with Fig. 3).

Therefore, the raw data of Fig. 4(a) become directly comparable and provide a measure of the spin-current amplitude injected into the Pt "detector layer". Figure 4(b) shows that the THz-signal strength (RMS) decreases with increasing d_1. The experimental curve can be very well fit by a monoexponential $\propto \exp(-d_1/\lambda_{\mathrm{rel}})$ with $\lambda_{\mathrm{rel}} = 4.0$ nm [see Fig. 4(b)]. We note that on one hand, this value of the THz-spin-current relaxation length in Cu is substantially larger than for metals with a sizeable SHE (see

Fig. 3). On the other hand, it is small compared to DC spin diffusion lengths, which are on the order of 100 nm in Cu (ref. 51).

Interestingly, we do not observe indications of a discontinuity around $d_1 = 0$ nm. The continuous behavior suggests similar spin-current transmission efficiencies through $Co_{40}Fe_{40}B_{20}$/Pt compared to $Co_{40}Fe_{40}B_{20}$/Cu and Cu/Pt interfaces. It has to be emphasized that this observation cannot be generalized and may, in contrast, strongly depend on materials and probe frequency. For example, recent gigahertz spin-pumping experiments on Co|Cu|Pt revealed a strong interface dependence of the spin-current transmission[32,33]. Nevertheless, we note that such kind of THz-spin-current-transmission experiments could be used to characterize any FM|NM interface involving metals. To conclude, the results of Fig. 4 support our THz emission model based on Eqs. (1) and (2) assuming minor impact of the FM|NM interface.

4.5. Extraction of the spin Hall angle

Now we have determined all relevant parameters in Eqs. (1) and (2) which allows us to extract the relative Θ_{SH}. Figure 5 shows raw data comparing FM|W and FM|$Cu_{80}Ir_{20}$ heterostructures with their respective Pt capped reference sample having an identical sample architecture (see Table 1). The absorptance of these references is 0.60 for $Co_{40}Fe_{40}B_{20}$(3nm)|Pt(3nm) and 0.61 for Fe(3) |Pt(4)|AlO_x(3).

The ratio $\Theta_{\mathrm{SH}}^{\mathrm{raw}}$ of the THz-signal amplitudes (RMS) of sample and reference are also given Fig.5. As shown in our previous work[19], $\Theta_{\mathrm{SH}}^{\mathrm{raw}}$ can already provide a reasonably robust estimate of the relative Θ_{SH}. However, as shown by Eq. (2), this notion holds only true if the studied materials have comparable properties in terms of pump-pulse absorptance, THz conductivity and THz spin current relaxation length (see Tables 2 and 3). Our detailed analysis finally allows us to fully account for these material parameters and to eventually extract the relative Θ_{SH}. Here, Pt serves as the reference since it is by far the most studied spintronic material with $\Theta_{\mathrm{SH}}^{\mathrm{Pt}} = 0.12$ (Ref. 40).

Table 3 is the key result of this work: It summarizes the measured values for λ_{rel} and Θ_{SH} and compares it to the directly extracted value from the raw data $\Theta_{\mathrm{SH}}^{\mathrm{raw}}$. When comparing to reported values for Θ_{SH}, we find very good agreement for $Cu_{80}Ir_{20}$ (2.1% in Ref. 38). For Tungsten, the conductivity (see Table 2) indicates an alpha crystal phase for which a Θ_{SH} of similar magnitude and sign has been reported[52,17].

5. Discussion

Although the raw THz-emission data in Fig. 5 already provide a reasonably robust estimate of the relative spin Hall angle (ref. 19), the direct comparison between Θ_{SH} and $\Theta_{\mathrm{SH}}^{\mathrm{raw}}$ (Table 2) clearly demonstrates the need for an advanced data analysis which is provided by Eqs. (1) and (2). If only the raw data is considered, different optical and THz material properties as well as a varying λ_{rel} may have a significant impact on the extracted Θ_{SH}. For instance, variations by a factor of almost 2 occur in the case of $Cu_{80}Ir_{20}$ (see Table 3).

We find good agreement between the conductivities and spintronic parameters measured by THz spectroscopy here and DC values measured by contact-based electrical schemes previously. This observation and a recent study[21] of the THz spin-Seebeck effect suggest that highly excited electrons play a minor role in the THz emission process and that thermalized electrons make the dominant contribution.

As the analysis presented here is based on our model of spin transport [Eq. (1)] and THz emission [Eq. (2)], it is important to recapitulate its assumptions and limitations. First, Eq. (2) is only applicable for thin metal films (thickness below 20 nm), thereby ensuring a homogenous optical excitation of the metal films and the validity of the thin-film approximation [Eq. (2)]. This condition is usually well fulfilled in

practice. Second, in our analysis, THz emission by the anomalous Hall effect in the FM layer has been neglected, which, however, appears to only lead to minor corrections[26].

Finally, the spin-current transmission coefficients through the FM/NM interfaces are assumed to be approximately equal for all NM metals considered here. This assumption is supported by measurements using a Cu intermediate layer, but it is certainly important to investigate spin transmission through interfaces for a broader set of materials and interface parameters. Nevertheless, the results of this study (see Table 3) clearly show that THz emission spectroscopy is a reliable tool for contactless all-optical spintronic material characterization with high sample throughput.

6. Conclusion

We present a detailed measurement and analysis scheme to establish TES as a reliable, fast and efficient all-optical method to probe spin-to-charge conversion on the femtosecond time scale. TES has several advantages: Importantly, it allows for a large sample throughput because of the relatively short measurement time which is only about 1 minute for a complete THz waveform of the presented material combinations. Moreover, this all-optical and contact-free approach is very versatile as it does not require any microstructuring. It even permits the investigation of discontinuous films such as thin gold films below the percolation threshold[53]. Furthermore, we present a promising experimental approach for FM/NM-interface characterization: THz-spin-current transmission measurements through a metal with negligibly small SHE. The good agreement of our measured spin Hall parameters with literature values suggests that thermalized electrons play a significant role in the THz-emission process. Finally, our results suggest copper-iridium alloys to be promising spin-to-charge-current-conversion materials. Future TES studies will also aim at quantifying the photon-to-spin conversion efficiency and the spin-current transmission through interfaces, eventually allowing for the determination of the absolute value of the spin Hall angle.

Acknowledgments

We acknowledge funding by the the DFG priority program SPP 1538 “SpinCaT”, the collaborative research centers SFB TRR 227 “Ultrafast spin dynamics” and SFB TRR 173 “Spin+X”, the ERC H2020 CoG project TERAMAG/Grant No. 681917 and the Graduate School of Excellence GSC266 “Materials Science in Mainz”.

References

[1] Chen, Y-T., and S. M. Xie. "Magnetic and electric properties of amorphous $Co_{40}Fe_{40}B_{20}$ thin films." *Journal of Nanomaterials* **2012** (2012): 29.

[2] Rossnagel, S. M., I. C. Noyan, and C. Cabral Jr. "Phase transformation of thin sputter-deposited tungsten films at room temperature." *Journal of Vacuum Science & Technology B: Microelectronics and Nanometer Structures Processing, Measurement, and Phenomena* **20** (2002): 2047-2051.

[3] Rubinstein, M., et al. "Electrical transport properties of thin epitaxially grown iron films." *Physical review B* **37** (1988): 8689.

[4] Keller, S., et al. "Determination of the spin Hall angle in single-crystalline Pt films from spin pumping experiments." *arXiv preprint* arXiv:1712.05334 (2017).

[5] Sander, D., et al. "The 2017 Magnetism Roadmap." *Journal of Physics D: Applied Physics* **50** (2017): 363001.

[6] Prenat, G., et al. "Beyond STT-MRAM, spin orbit torque RAM SOT-MRAM for high speed and high reliability applications." Spintronics-based Computing. Springer, Cham, 2015. 145-157.
[7] Miron, I. M., et al. "Perpendicular switching of a single ferromagnetic layer induced by in-plane current injection." *Nature* **476** (2011): 189.
[8] Prenat, G., et al. "Ultra-fast and high-reliability SOT-MRAM: from cache replacement to normally-off computing." *IEEE Transactions on Multi-Scale Computing Systems* **2** (2016): 49-60.
[9] Hirsch, J. E. "Spin hall effect." *Physical review letters* **83** (1999): 1834.
[10] Sinova, J., et al. "Spin hall effects." *Reviews of modern physics* **87** (2015): 1213.
[11] Niimi, Y., and Y. Otani. "Reciprocal spin Hall effects in conductors with strong spin–orbit coupling: a review." *Reports on progress in physics* **78** (2015): 124501.
[12] Saitoh, E., et al. "Conversion of spin current into charge current at room temperature: Inverse spin-Hall effect." *Applied physics letters* **88** (2006): 182509.
[13] Liu, L., et al. "Spin-torque ferromagnetic resonance induced by the spin Hall effect." *Physical review letters* **106** (2011): 036601.
[14] Wen, Y., et al. "Temperature dependence of spin-orbit torques in Cu-Au alloys." *Physical review B* **95** (2017): 104403.
[15] Smits, F. M. "Measurement of sheet resistivities with the four-point probe." *Bell Labs Technical Journal* **37** (1958): 711-718.
[16] Berger, A. J., et al. "Inductive detection of fieldlike and dampinglike ac inverse spin-orbit torques in ferromagnet/normal-metal bilayers." *Physical review B* **97** (2018): 094407.
[17] Mondal, S., et al. "All-optical detection of the spin Hall angle in W/CoFeB/SiO 2 heterostructures with varying thickness of the tungsten layer." *Physical review B* **96** (2017): 054414.
[18] Kampfrath, T., et al. "Terahertz spin current pulses controlled by magnetic heterostructures." *Nature nanotechnology* **8** (2013): 256.
[19] Seifert, T., et al. "Efficient metallic spintronic emitters of ultrabroadband terahertz radiation." *Nature photonics* **10** (2016): 483-488.
[20] Seifert, T., et al. "Terahertz spin currents and inverse spin Hall effect in thin-film heterostructures containing complex magnetic compounds." *Spin* **7**, World Scientific Publishing Company, 2017.
[21] Seifert, T., et al. " Femtosecond formation dynamics of the spin Seebeck effect revealed by terahertz spectroscopy." *arXiv preprint* arXiv:1709.00768 (2017).
[22] Leitenstorfer, A., et al. "Detectors and sources for ultrabroadband electro-optic sampling: Experiment and theory." *Applied physics letters* **74** (1999): 1516-1518.
[23] Kampfrath, T., J. Nötzold, and M. Wolf. "Sampling of broadband terahertz pulses with thick electro-optic crystals." *Applied Physics Letters* **90** (2007): 231113.
[24] Ganichev, S. D., et al. "Spin-galvanic effect." *Nature* **417** (2002): 153.
[25] Seifert, T., et al. "Ultrabroadband single-cycle terahertz pulses with peak fields of 300 kV cm^{-1} from a metallic spintronic emitter." *Applied Physics Letters* **110** (2017): 252402.
[26] Wu, Y., et al. "High-Performance THz Emitters Based on Ferromagnetic/Nonmagnetic Heterostructures." *Advanced Materials* **29** (2017).
[27] Yang, D., et al. "Powerful and tunable THz emitters based on the Fe/Pt magnetic heterostructure." *Advanced Optical Materials* **4** (2016): 1944-1949.
[28] Sasaki, Y., K. Z. Suzuki, and S. Mizukami. "Annealing effect on laser pulse-induced THz wave emission in Ta/CoFeB/MgO films." *Applied physics letters* **111** (2017): 102401.
[29] Torosyan, G., et al. "Optimized Spintronic Terahertz Emitters Based on Epitaxial Grown Fe/Pt Layer Structures." *Scientific reports* **8** (2018): 1311.
[30] Stamm, C., et al. "Magneto-Optical Detection of the Spin Hall Effect in Pt and W Thin Films." *Physical review letters* **119** (2017): 087203.
[31] Aeschlimann, M., et al. "Ultrafast spin-dependent electron dynamics in fcc Co." *Physical review letters* **79** (1997): 5158.

[32] Rojas-Sánchez, J-C., et al. "Spin pumping and inverse spin Hall effect in platinum: the essential role of spin-memory loss at metallic interfaces." *Physical review letters* **112** (2014): 106602.
[33] Zhang, W., et al. "Role of transparency of platinum–ferromagnet interfaces in determining the intrinsic magnitude of the spin Hall effect." *Nature physics* **11** (2015): 496.
[34] Huisman, T. J., et al. "Spin-photo-currents generated by femtosecond laser pulses in a ferrimagnetic GdFeCo/Pt bilayer." *Applied physics letters* **110** (2017): 072402.
[35] Li, G., et al. "Laser induced THz emission from femtosecond photocurrents in Co/ZnO/Pt and Co/Cu/Pt multilayers." *Journal of Physics D: Applied Physics* (2018).
[36] Zhang, S., et al. "Photoinduced terahertz radiation and negative conductivity dynamics in Heusler alloy Co_2MnSn film." *Optics letters* **42** (2017): 3080-3083.
[37] Huisman, T. J., et al. "Femtosecond control of electric currents in metallic ferromagnetic heterostructures." *Nature nanotechnology* **11** (2016): 455.
[38] Niimi, Y., et al. "Extrinsic spin Hall effect induced by iridium impurities in copper." *Physical review letters* **106** (2011): 126601.
[39] Cramer, J., et al. "Complex Terahertz and Direct Current Inverse Spin Hall Effect in YIG/Cu_{1-x} Ir_x Bilayers Across a Wide Concentration Range." *Nano letters* **18** (2018): 1064-1069.
[40] Obstbaum, M., et al. "Inverse spin Hall effect in Ni_{81} Fe_{19}/normal-metal bilayers." *Physical Review B* **89** (2014): 060407.
[41] Duvillaret, L., F. Garet, and J-L. Coutaz. "A reliable method for extraction of material parameters in terahertz time-domain spectroscopy." *IEEE Journal of selected topics in quantum electronics* **2** (1996): 739-746.
[42] Leitenstorfer, A., et al. "Femtosecond charge transport in polar semiconductors." *Physical review letters* **82** (1999): 5140.
[43] Braun, L., et al. "Ultrafast photocurrents at the surface of the three-dimensional topological insulator Bi_2Se_3." *Nature communications* **7** (2016): 13259.
[44] Nattermann, T., Y. Shapir, and I. Vilfan. "Interface pinning and dynamics in random systems." *Physical review B* **42** (1990): 8577.
[45] Duvillaret, L., F. Garet, and J-L. Coutaz. "Highly precise determination of optical constants and sample thickness in terahertz time-domain spectroscopy." *Applied optics* **38** (1999): 409-415.
[46] Krewer, K. L., et al. "Accurate terahertz spectroscopy of supported thin films by precise substrate thickness correction." *Optics letters* **43** (2018): 447-450.
[47] Fuchs, K. "The conductivity of thin metallic films according to the electron theory of metals." *Mathematical Proceedings of the Cambridge Philosophical Society* **34**, Cambridge University Press, 1938.
[48] Valet, T., and A. Fert. "Theory of the perpendicular magnetoresistance in magnetic multilayers." *Physical review B* **48** (1993): 7099.
[49] Jedema, Friso Jacobus, A. T. Filip, and B. J. Van Wees. "Electrical spin injection and accumulation at room temperature in an all-metal mesoscopic spin valve." *Nature* **410** (2001): 345.
[50] Ilgaz, Dennis, et al. "Domain-wall depinning assisted by pure spin currents." *Physical review letters* **105** (2010): 076601.
[51] Piraux, Luc, S. Dubois, and A. Fert. "Perpendicular giant magnetoresistance in magnetic multilayered nanowires." *Journal of magnetism and magnetic materials* **159** (1996): 287-292.
[52] Pai, C-F., et al. "Spin transfer torque devices utilizing the giant spin Hall effect of tungsten." *Applied physics letters* **101** (2012): 122404.
[53] Walther, M., et al. "Terahertz conductivity of thin gold films at the metal-insulator percolation transition." *Physical review B* **76** (2007): 125408.